Research Article | Vol. 8, No. 3 | 1 Mar 2017 | BIOMEDICAL OPTICS EXPRESS 1290
Biomedical Optics EXPRESS

Three-dimensional multi-contrast imaging of in vivo human skin by Jones matrix optical coherence tomography

EN LI,[1,2] SHUICHI MAKITA,[1,2] YOUNG-JOO HONG,[1,2] DEEPA KASARAGOD,[1,2] AND YOSHIAKI YASUNO[1,2,*]

[1] *Computational Optics Group, University of Tsukuba, Tennodai 1-1-1, Tsukuba, Ibaraki, 305-8573, Japan*
[2] *Computational Optics and Ophthalmology Group, Tsukuba, Ibaraki, Japan*
[*] *yasuno@optlab2.bk.tsukuba.ac.jp*
http://optics.bk.tsukuba.ac.jp/COG/

Abstract: A custom made dermatological Jones matrix optical coherence tomography (JM-OCT) is presented. It uses a passive-polarization-delay component based swept-source JM-OCT configuration, but is specially designed for *in vivo* human skin measurement. The center wavelength of its probe beam is 1310 nm and the A-line rate is 49.6 kHz. The JM-OCT is capable of simultaneously providing birefringence (local retardation) tomography, degree-of-polarization-uniformity tomography, complex-correlation-based optical coherence angiography, and conventional scattering OCT. To evaluate the performance of this JM-OCT, we measured *in vivo* human skin at several locations. Using the four kinds of OCT contrasts, the morphological characteristics and optical properties of different skin types were visualized.

OCIS codes: (170.4500) Optical coherence tomography; (110.4500) Optical coherence tomography; (110.5405) Polarimetric imaging; (170.1870) Dermatology.

References and links

1. D. Huang, E. A. Swanson, C. P. Lin, J. S. Schuman, W. G. Stinson, W. Chang, M. R. Hee, T. Flotte, K. Gregory, C. A. Puliafito, and J. G. Fujimoto, "Optical coherence tomography," Science **254**, 1178–1181 (1991).
2. J. A. Izatt, M. R. Hee, E. A. Swanson, C. P. Lin, D. Huang, J. S. Schuman, C. A. Puliafito, and J. G. Fujimoto, "Micrometer-scale resolution imaging of the anterior eye in vivo with optical coherence tomography," Arch. Ophthalmol. **112**, 1584–1589 (1994).
3. C. A. Puliafito, M. R. Hee, C. P. Lin, E. Reichel, J. S. Schuman, J. S. Duker, J. A. Izatt, E. A. Swanson, and J. G. Fujimoto, "Imaging of macular diseases with optical coherence tomography," Ophthalmology **102**, 217–229 (1995).
4. I.-K. Jang, G. J. Tearney, B. MacNeill, M. Takano, F. Moselewski, N. Iftima, M. Shishkov, S. Houser, H. T. Aretz, E. F. Halpern, and B. E. Bouma, "In vivo characterization of coronary atherosclerotic plaque by use of optical coherence tomography," Circulation **111**, 1551–1555 (2005).
5. G. J. Tearney, M. E. Brezinski, J. F. Southern, B. E. Bouma, S. A. Boppart, and J. G. Fujimoto, "Optical biopsy in human gastrointestinal tissue using optical coherence tomography," Am. J. Gastroenterol. **92**, 1800–1804 (1997).
6. B. W. Colston, U. S. Sathyam, L. B. DaSilva, M. J. Everett, P. Stroeve, and L. L. Otis, "Dental OCT," Opt. Express **3**, 230–238 (1998).
7. J. Welzel, E. Lankenau, R. Birngruber, and R. Engelhardt, "Optical coherence tomography of the human skin," J. Am. Acad. Dermatol. **37**, 958–963 (1997).
8. J. Welzel, "Optical coherence tomography in dermatology: a review," Skin Res. Technol. **7**, 1–9 (2001).
9. T. Gambichler, G. Moussa, M. Sand, D. Sand, P. Altmeyer, and K. Hoffmann, "Applications of optical coherence tomography in dermatology," J. Dermatol. Sci. **40**, 85–94 (2005).
10. E. Auksorius and A. C. Boccara, "Fingerprint imaging from the inside of a finger with full-field optical coherence tomography," Biomed. Opt. Express **6**, 4465–4471 (2015).
11. E. Harris and A. Sjoerdsma, "Effect of penicillamine on human collagen and its possible application to treatment of scleroderma," Lancet **288**, 996–999 (1966).
12. G. P. Rodnan, E. Lipinski, and J. Luksick, "Skin thickness and collagen content in progressive systemic sclerosis and localized scleroderma," Arthritis Rheumatol. **22**, 130–140 (1979).
13. G. Rayman, A. Hassan, and J. E. Tooke, "Blood flow in the skin of the foot related to posture in diabetes mellitus," Br. Med. J. (Clin. Res. Ed.) **292**, 87–90 (1986).
14. G. Belcaro, S. Vasdekis, A. Rulo, and A. N. Nicolaides, "Evaluation of skin blood flow and venoarteriolar response in patients with diabetes and peripheral vascular disease by laser doppler flowmetry," Angiology **40**, 953–957 (1989).

#283499 https://doi.org/10.1364/BOE.8.001290
Journal © 2017 Received 22 Dec 2016; revised 28 Jan 2017; accepted 30 Jan 2017; published 1 Feb 2017

Biomedical Optics EXPRESS

15. J. A. Izatt, M. D. Kulkarni, S. Yazdanfar, J. K. Barton, and A. J. Welch, "In vivo bidirectional color Doppler flow imaging of picoliter blood volumes using optical coherence tomography," Opt. Letters **22**, 1439–1441 (1997).
16. J. F. d. Boer, S. M. Srinivas, A. Malekafzali, Z. Chen, and J. S. Nelson, "Imaging thermally damaged tissue by polarization sensitive optical coherence tomography," Opt. Express **3**, 212–218 (1998).
17. Y. Yasuno, S. Makita, Y. Sutoh, M. Itoh, and T. Yatagai, "Birefringence imaging of human skin by polarization-sensitive spectral interferometric optical coherence tomography," Opt. Letters **27**, 1803–1805 (2002).
18. M. C. Pierce, J. Strasswimmer, B. Hyle Park, B. Cense, and J. F. de Boer, "Advances in optical coherence tomography imaging for dermatology," J. Invest. Dermatol. **123**, 458–463 (2004).
19. S. Sakai, M. Yamanari, A. Miyazawa, M. Matsumoto, N. Nakagawa, T. Sugawara, K. Kawabata, T. Yatagai, and Y. Yasuno, "In vivo three-dimensional birefringence analysis shows collagen differences b etween young and old photo-aged human skin," J. Invest. Dermatol. **128**, 1641–1647 (2008).
20. W. J. Choi, R. Reif, S. Yousefi, and R. K. Wang, "Improved microcirculation imaging of human skin in vivo using optical microangiography with a correlation mapping mask," J. of Biomed. Opt. **19**, 036010 (2014).
21. B. Park, M. C. Pierce, B. Cense, S.-H. Yun, M. Mujat, G. Tearney, B. Bouma, and J. de Boer, "Real-time fiber-based multi-functional spectral-domain optical coherence tomography at 1.3 μm," Opt. Express **13**, 3931–3944 (2005).
22. S. Sugiyama, Y.-J. Hong, D. Kasaragod, S. Makita, S. Uematsu, Y. Ikuno, M. Miura, and Y. Yasuno, "Birefringence imaging of posterior eye by multi-functional Jones matrix optical coherence tomography," Biomed. Opt. Express **6**, 4951–4974 (2015).
23. S. Guo, J. Zhang, L. Wang, J. S. Nelson, and Z. Chen, "Depth-resolved birefringence and differential optical axis orientation measurements with fiber-based polarization-sensitive optical coherence tomography," Opt. Lett. **29**, 2025–2027 (2004).
24. S. Makita, M. Yamanari, and Y. Yasuno, "Generalized jones matrix optical coherence tomography: performance and local birefringence imaging," Opt. Express **18**, 854–876 (2010).
25. D. Kasaragod, S. Makita, S. Fukuda, S. Beheregaray, T. Oshika, and Y. Yasuno, "Bayesian maximum likelihood estimator of phase retardation for quantitative polarization-sensitive optical coherence tomography," Opt. Express **22**, 16472–16492 (2014).
26. Y. Lim, M. Yamanari, S. Fukuda, Y. Kaji, T. Kiuchi, M. Miura, T. Oshika, and Y. Yasuno, "Birefringence measurement of cornea and anterior segment by office-based polarization-sensitive optical coherence tomography," Biomed. Opt. Express **2**, 2392–2402 (2011).
27. M. J. Ju, Y.-J. Hong, S. Makita, Y. Lim, K. Kurokawa, L. Duan, M. Miura, S. Tang, and Y. Yasuno, "Advanced multi-contrast Jones matrix optical coherence tomography for Doppler and polarization sensitive imaging," Opt. Express **21**, 19412–19436 (2013).
28. M. Yamanari, S. Tsuda, T. Kokubun, Y. Shiga, K. Omodaka, Y. Yokoyama, N. Himori, M. Ryu, S. Kunimatsu-Sanuki, H. Takahashi, K. Maruyama, H. Kunikata, and T. Nakazawa, "Fiber-based polarization-sensitive OCT for birefringence imaging of the anterior eye segment," Biomed. Opt. Express **6**, 369–389 (2015).
29. Z. Wang, H.-C. Lee, O. O. Ahsen, B. Lee, W. Choi, B. Potsaid, J. Liu, V. Jayaraman, A. Cable, M. F. Kraus, K. Liang, J. Hornegger, and J. G. Fujimoto, "Depth-encoded all-fiber swept source polarization sensitive OCT," Biomed. Opt. Express **5**, 2931–2949 (2014).
30. M. Yamanari, S. Tsuda, T. Kokubun, Y. Shiga, K. Omodaka, N. Aizawa, Y. Yokoyama, N. Himori, S. Kunimatsu-Sanuki, K. Maruyama, H. Kunikata, and T. Nakazawa, "Estimation of jones matrix, birefringence and entropy using cloude-pottier decomposition in polarization-sensitive optical coherence tomography," Biomed. Opt. Express **7**, 3551–3573 (2016).
31. M. Villiger and B. E. Bouma, "Practical decomposition for physically admissible differential Mueller matrices," Opt. Lett. **39**, 1779–1782 (2014).
32. M. Villiger, D. Lorenser, R. A. McLaughlin, B. C. Quirk, R. W. Kirk, B. E. Bouma, and D. D. Sampson, "Deep tissue volume imaging of birefringence through fibre-optic needle probes for the delineation of breast tumour," Sci. Rep. **6**, 28771 (2016).
33. L. Duan, S. Makita, M. Yamanari, Y. Lim, and Y. Yasuno, "Monte-Carlo-based phase retardation estimator for polarization sensitive optical coherence tomography," Opt. Express **19**, 16330–16345 (2011).
34. D. Kasaragod, S. Sugiyama, Y. Ikuno, D. Alonso-Caneiro, M. Yamanari, S. Fukuda, T. Oshika, Y.-J. Hong, E. Li, S. Makita, M. Miura, and Y. Yasuno, "Accurate and quantitative polarization-sensitive oct by unbiased birefringence estimator with noise-stochastic correction," Proc. SPIE **9697**, 96971I (2016).
35. D. Kasaragod, S. Makita, Y.-J. Hong, and Y. Yasuno, "Noise stochastic corrected maximum a posteriori estimator for birefringence imaging using polarization-sensitive optical coherence tomography," Biomed. Opt. Express **8**, 653–669 (2017).
36. M. Bonesi, H. Sattmann, T. Torzicky, S. Zotter, B. Baumann, M. Pircher, E. Goetzinger, C. Eigenwillig, W. Wieser, R. Huber, and C. K. Hitzenberger, "High-speed polarization sensitive optical coherence tomography scan engine based on Fourier domain mode locked laser," Biomed. Opt. Express **3**, 2987–3000 (2012).
37. W. C. Y. Lo, M. Villiger, A. Golberg, G. F. Broelsch, S. Khan, C. G. Lian, W. G. Austen, M. Yarmush, and B. E. Bouma, "Longitudinal, 3d Imaging of Collagen Remodeling in Murine Hypertrophic Scars In Vivo Using Polarization-Sensitive Optical Frequency Domain Imaging," J. Invest. Dermatol. **136**, 84–92 (2016).
38. G. Liu, W. Jia, V. Sun, B. Choi, and Z. Chen, "High-resolution imaging of microvasculature in human skin in-vivo with optical coherence tomography," Opt. Express **20**, 7694–7705 (2012).

Biomedical Optics EXPRESS

39. W. J. Choi and R. K. Wang, "Volumetric cutaneous microangiography of human skin in vivo by vcsel swept-source optical coherence tomography," Quantum Electron. **44**, 740 (2014).
40. E. Götzinger, M. Pircher, W. Geitzenauer, C. Ahlers, B. Baumann, S. Michels, U. Schmidt-Erfurth, and C. K. Hitzenberger, "Retinal pigment epithelium segmentation by polarization sensitive optical coherence tomography," Opt. Express **16**, 16410–16422 (2008).
41. S. Makita, Y.-J. Hong, M. Miura, and Y. Yasuno, "Degree of polarization uniformity with high noise immunity using polarization-sensitive optical coherence tomography," Opt. Lett. **39**, 6783–6786 (2014).
42. S. Makita, K. Kurokawa, Y.-J. Hong, M. Miura, and Y. Yasuno, "Noise-immune complex correlation for optical coherence angiography based on standard and Jones matrix optical coherence tomography," Biomed. Opt. Express **7**, 1525–1548 (2016).
43. B. Baumann, W. Choi, B. Potsaid, D. Huang, J. S. Duker, and J. G. Fujimoto, "Swept source / Fourier domain polarization sensitive optical coherence tomography with a passive polarization delay unit," Opt. Express **20**, 10229–10241 (2012).
44. Y. Lim, Y.-J. Hong, L. Duan, M. Yamanari, and Y. Yasuno, "Passive component based multifunctional Jones matrix swept source optical coherence tomography for Doppler and polarization imaging," Opt. Lett. **37**, 1958–1960 (2012).
45. S. Makita and Y. Yasuno, "In vivo photothermal optical coherence tomography for non-invasive imaging of endogenous absorption agents," Biomed. Opt. Express **6**, 1707–1725 (2015).
46. S. Moon, S.-W. Lee, and Z. Chen, "Reference spectrum extraction and fixed-pattern noise removal in optical coherence tomography," Opt. Express **18**, 24395–24404 (2010).
47. W. F. H. A. Text and C. Atlas, *Wheater's Functional Histology: A Text and Colour Atlas* (Churchill Livingstone, 2013), 6th ed.
48. M. Pircher, E. Goetzinger, R. Leitgeb, and C. K. Hitzenberger, "Three dimensional polarization sensitive OCT of human skin in vivo," Opt. Express **12**, 3236–3244 (2004).
49. G. Liu and Z. Chen, "Capturing the vital vascular fingerprint with optical coherence tomography," Appl. Opt. **52**, 5473–5477 (2013).
50. A. Zam, R. Dsouza, H. M. Subhash, M.-L. O'Connell, J. Enfield, K. Larin, and M. J. Leahy, "Feasibility of correlation mapping optical coherence tomography (cmoct) for anti-spoof sub-surface fingerprinting," J. Biophotonics **6**, 663–667 (2013).
51. J. T. Whitton and J. Everall, "The thickness of the epidermis," Br. J. Dermatol. **89**, 467–476 (1973).
52. S. Sakai, M. Yamanari, Y. Lim, N. Nakagawa, and Y. Yasuno, "In vivo evaluation of human skin anisotropy by polarization-sensitive optical coherence tomography," Biomed. Opt. Express **2**, 2623–2631 (2011).
53. M. Bonesi, M. P. Minneman, J. Ensher, B. Zabihian, H. Sattmann, P. Boschert, E. Hoover, R. A. Leitgeb, M. Crawford, and W. Drexler, "Akinetic all-semiconductor programmable swept-source at 1550 nm and 1310 nm with centimeters coherence length," Opt. Express **22**, 2632–2655 (2014).
54. O. O. Ahsen, Y. K. Tao, B. M. Potsaid, Y. Sheikine, J. Jiang, I. Grulkowski, T.-H. Tsai, V. Jayaraman, M. F. Kraus, J. L. Connolly, J. Hornegger, A. Cable, and J. G. Fujimoto, "Swept source optical coherence microscopy using a 1310 nm VCSEL light source," Opt. Express **21**, 18021–18033 (2013).
55. Y. Yasuno, J. ichiro Sugisaka, Y. Sando, Y. Nakamura, S. Makita, M. Itoh, and T. Yatagai, "Non-iterative numerical method for laterally superresolving fourier domain optical coherence tomography," Opt. Express **14**, 1006–1020 (2006).
56. T. S. Ralston, D. L. Marks, P. Scott Carney, and S. A. Boppart, "Interferometric synthetic aperture microscopy," Nature Phys. **3**, 129–134 (2007).
57. A. Kumar, W. Drexler, and R. A. Leitgeb, "Numerical focusing methods for full field oct: a comparison based on a common signal model," Opt. Express **22**, 16061–16078 (2014).
58. J. Mo, M. de Groot, and J. F. de Boer, "Focus-extension by depth-encoded synthetic aperture in optical coherence tomography," Opt. Express **21**, 10048–10061 (2013).
59. R. A. Leitgeb, M. Villiger, A. H. Bachmann, L. Steinmann, and T. Lasser, "Extended focus depth for fourier domain optical coherence microscopy," Opt. Lett. **31**, 2450–2452 (2006).
60. A. Bouwens, T. Bolmont, D. Szlag, C. Berclaz, and T. Lasser, "Quantitative cerebral blood flow imaging with extended-focus optical coherence microscopy," Opt. Lett. **39**, 37–40 (2014).
61. M. Villiger, J. Goulley, M. Friedrich, A. Grapin-Botton, P. Meda, T. Lasser, and R. A. Leitgeb, "In vivo imaging of murine endocrine islets of langerhans with extended-focus optical coherence microscopy," Diabetologia **52**, 1599–1607 (2009).

1. Introduction

Optical coherence tomography (OCT) is a noninvasive, high resolution, and fast imaging modality that is capable of visualizing the internal micro-structures of *in vivo* tissue [1]. Because of these particular advantages, OCT has been applied in several medical fields such as ophthalmology [2, 3], cardiology [4], gastroenterology [5], dentistry [6], and dermatology [7–10]. Among them, dermatology is a suitable field for OCT because skin is easily accessible and

Biomedical Optics EXPRESS

consists of several sub-millimeter internal structures.

Skin consists of a significant amount of collagen, which is a birefringent material. In addition, some skin diseases, such as scleroderma, are believed to be associated with collagen abnormality [11, 12]. Hence, birefringence measurement would be useful for pathological investigation. Futhermore, some research has found that skin blood flow relates to diabetes and peripheral vascular disease [13, 14]. This suggests that non-invasive angiography would be able to provide useful information for diagnosing diabetes and vascular disease.

There are some functional extensions of OCT that have been applied to dermatological investigations [15–20]. Among them, polarization sensitive OCT (PS-OCT) [16, 17, 19], OCT angiography (OCT-A) [15], and its combination [21] are the most promising options. Currently, most dermatological PS-OCT measures phase retardation to detect the polarization property of the skin. However, it was recently argued that the phase retardation measurement is not accurate for biological tissues with non-uniform optic axis orientation along its depth, which includes skin [22]. Therefore, a depth-localized birefringence measurement is required for more accurate dermatological investigation. The limitation of cumulative phase retardation imaging can be overcome by the birefringence measurement based on localized Jones matrix measurement [23–25]. Although the local Jones matrix measurement suffers from a low signal-to-noise ratio and inaccurate phase-retardation and birefringence, these problems were recently resolved by birefringence and phase retardation estimation techniques that include the coherent averaging of the Jones matrix and/or Jones vector [26–28], eigen-value-based averaging [29], Jones matrix estimation based on the Cloude-Pottier decomposition [30], Muller analysis [31, 32], a specially designed phase-retardation estimation function [33], and maximum *a posteriori* birefringence estimators [25, 34, 35]. These advances enabled the birefringence imaging of *in vivo* skin. The uniformity of polarization property of tissue is also useful for dermatological investigation [36]. It was recently applied to investigate hypertrophic scars [37]. OCT-A has also been applied to dermatological investigations. This method enables the non-invasive visualization of the internal vascular structure *in vivo* [38, 39]

In this paper, we demonstrate our new multifunctional (multi-contrast) Jones matrix optical coherence tomography (JM-OCT) for dermatological imaging. It enables the simultaneous investigation of the polarization and flow properties of skin. The JM-OCT simultaneously provides depth-resolved birefringence (local phase retardation) tomography [25], degree-of-polarization-uniformity (DOPU) [40, 41], complex-correlation based OCT-A [42], and the scattering intensity OCT. The system is based on a design that is similar to our previous passive-polarization-delay based posterior-eye JM-OCT [22, 27], but is specially redesigned for dermatological investigation. The performance of the system is demonstrated by measuring different skin tissues *in vivo*.

2. Method

2.1. Jones matrix OCT system

The dermatological JM-OCT system was built from the passive-polarization-delay-based PS-OCT [22, 27, 28, 43, 44]. The schematic of our JM-OCT is shown in Fig. 1(a). The light source is a MEMS-based wavelength sweeping laser source (AXA10823-8, Axsun Technologies, MA) with a center wavelength of 1310 nm, an average output power of 22.6 mW, and a scanning rate of 49,600 Hz. The light is first divided by a 90:10 broadband coupler (FC1310-70-10-APC, Thorlabs Inc., NJ) such that 90% goes to the sample arm, and the other 10% goes to the reference arm.

In the sample arm, the beam goes to a passive polarization delay (PPD) module. The PPD module used in this system has a configuration that is similar to the one in [22, 27], but all the optical components are miniaturized and encased in a small box (91 mm × 50 mm foot print and 30 mm height). This compact PPD module (DE-G043-13, Optohub Co. Ltd., Saitama, Japan)

Biomedical Optics EXPRESS

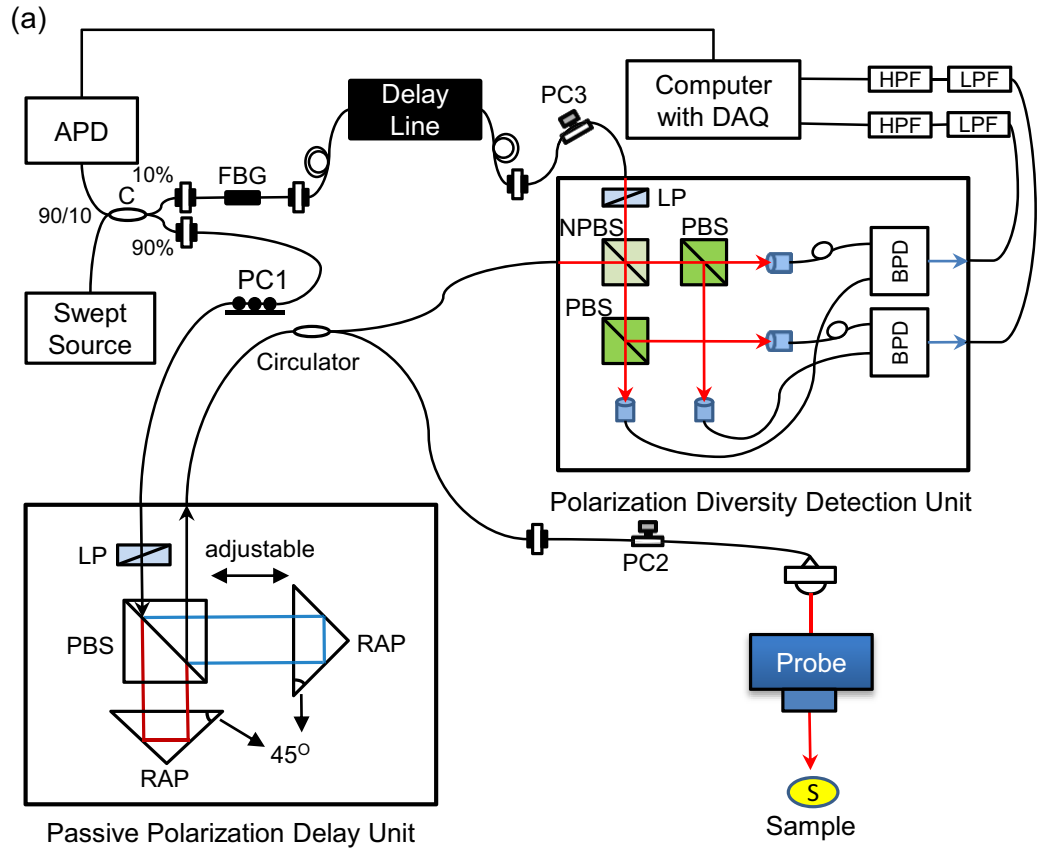

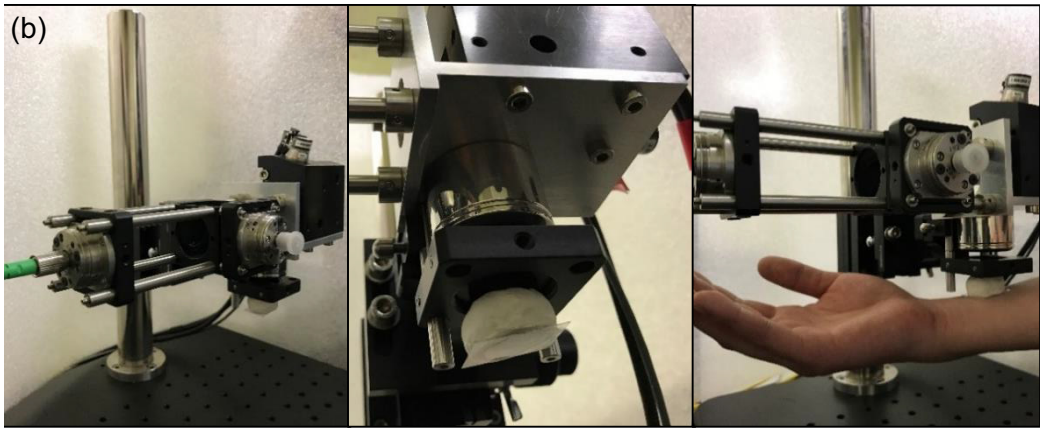

Fig. 1. (a) Configuration of the Jones matrix OCT system. APD: amplified photodetector; C: coupler; PC1, PC2 and PC3: polarization controllers; LP: linear polarizer; PBS: polarizing beam splitter; RAP: right angle prism; S: sample; NPBS: non-polarization beam splitter; BPD: balanced photodetetor; LPF: low pass filter, and HPF: high pass filter. (b) Pictures of scanning probe for skin.

Biomedical Optics EXPRESS

was collaboratively developed with Optohub Co. Ltd. and is commercially available. In the PPD module, the beam is split into two orthogonal independent polarizations states by a broadband polarizing beam-splitter cube (PBS). A linear polarizer is placed just before the PBS to control the splitting ratio. The split beams are recombined by another PBS and sent to the fiber output of the PPD module. Different delays are applied to the two polarizations before recombination. This mutual delay results in the depth-multiplexing of the two incident polarizations in the resulting OCT image [22,27]. The output power of the PPD is maximized by a fiber polarization controller just before the PPD module (PC1), i.e., just before the polarizer. The output from the PPD module goes to a bulk probe arm through a broadband circulator (CIR-1310-50-APC, Thorlabs). The back scattered light from the sample passes a polarization controller (PC2) and the circulator, and is sent to a polarization-diversity-detection module (PD-detector, DE-G036-13, Optohub).

In the probe unit, the beam is first collimated by a fiber-tip collimator (beam diameter = 3.49 mm, type number PAF-X-18-C, Thorlabs), passes a two dimensional galvanometric scanner (model 6220, Cambridge Technology Inc., MA), and focused by an objective (effective focal length = 36 mm, working distance = 25.1 mm, type number LSM03, Thorlabs). The $1/e^2$ beam diameter at the beam waist is 18 μm and the depth of focus is 389 μm. To reduce the skin surface reflection causing signal saturation, a tilted glass slip was attached in front of the probe unit as shown in Fig. 1(b). The space between the glass slip and the sample (skin) is filled by the ultrasound gel for refractive index matching. The incident power to the sample is around 10.2 mW. The probe unit is identical to that used in Ref. [45].

In addition, 10% of the power from the light source is sent to the reference arm of the interferometer. In the reference arm, the light is first sent to a fiber Bragg grating (FBG, FBG-SMF-1266-80-0.2-A-(2)60F/E, L = 1M, reflectivity $\geqslant$ 80%, Tatsuta Electric Wire & Cable Co., Ltd, Osaka, Japan). The light is reflected sharply at 1266-nm, and the reflected light is detected by a amplified photo-detector (PDA10CF, Thorlabs). The amplified photo-detector output is sent to a digitizer (ATS9350, Alazar Technologies Inc., Quebec, Canada) and used as a trigger for each A-line acquisition. The light passing the FBG goes to the reference arm, and is sent to the PD-detector through a variable optical delay line (Advanced Fiber Resource Ltd., Hong Kong, China.).

In the PD-detector, the reference and probe beams are combined by a non-polarization beam splitter (NPBS) and generate an interference signal. The interference signal is split into two polarization components by two PBSs, and these polarization components are independently detected by two balanced photo-detectors. In the reference path of the PD-detector, a polarizer is located just before the NPBS, which balances the reference powers between the two detection polarization channels. The total reference power is optimized by a polarization controller just before the PD-detector (PC3). In contrast to our previous JM-OCTs [22,27,44], the PD-detector in the present system is an encased detection module with a compact size of 156 mm (width) $\times$ 105 mm (depth) $\times$ 34 mm (height), which includes not only miniaturized bulk optics but also two balanced photo-detectors. Because of the encased PD-detector and PPD module, the system is built using only non-bulk components except for the probe head.

The detected interference signals are sent to the digitizer after passing through a high-pass filter (1 MHz cutoff frequency, Chebyshev type, HP1CH3, R&K Co., Ltd., Shizuoka,Japan) and a low-pass filter (62 MHz cutoff frequency, Chebyshev Type, LP62CH3, R&K Co., Ltd., Shizuoka, Japan) of each channel of the two output . Each spectral interference signal is sampled at 1,152 points and the optical bandwidth to be sampled is 106 nm. The sampling is performed with a built-in k-clock generated by the light source.

The OCT signals are generated from the Fourier transform of the intereference signals. Fixed pattern noise was removed by complex median subtraction method [46]. Because two incident polarizations are multiplexed by the PPD and two detection polarizations are independently detected by the PD-detector, this process provides a set of four complex OCT images. This set of

Biomedical Optics EXPRESS

OCT images forms a Jones matrix tomography, which is mathematically similar to the round trip Jones matrix of the sample. The Jones matrix tomography formation is identical to the process described in our previous publications [22, 27], but with the following exceptions. In the present system, we apply intensity correlation based sub-pixel depth-shift correction among four images, which was not used in the previous JM-OCT. For this sub-pixel shift, each intensity image of four polarization channels are enlarged along the depth with fast Fourier transform (FFT) based interpolation algorithm with 7-times of zero-padding. 1-D image correlations along the depth are computed among the four images. This correlation provides depth-shifts of each A-line. The shift between images is then defined as the median of the set of depth-shifts. In contrast, the numerical phase stabilization that is used in the previous system is not applied here because the phase has been stabilized by the k-clock.

The sensitivities of the four polarization channels were measured to be 105, 105, 104, and 104 dB. The depth imaging range is around 2.5 mm in air, which corresponds to 1.8 mm in tissue assuming a refractive index of 1.38. The axial resolution was measured to be 19.4 μm in air (14.1 μm in tissue), and the depth pixel separation was 8.7 μm in air (6.3 μm in tissue).

2.2. In vivo measurement protocol

To assess the utility of the JM-OCT for dermatological investigation, five healthy volunteers (4 males and 1 female) were measured. All the subjects are East Asian, and their ages ranged from 30 to 40 years old. For each subject, skin at three locations including finger pad, inner-forearm and outer-forearm were measured. Since the JM-OCT findings are consistent among the subjects, a representative case is discussed for each locations in Section 3.

The scan is a raster scan with 512 A-lines $\times$ 128 B-scans $\times$ 4 repeats of the B-scan. The imaging range is 6.0 $\times$ 6.0 mm in lateral and 1.8 mm in depth. For this configuration, the voxel size is 11.7 μm $\times$ 46.9 μm (lateral) $\times$ 6.3 μm (depth, in tissue). The acquisition time for a volume is 6.7 s.

All protocols were approved by the Institutional Review Board of the University of Tsukuba. Written informed consent was obtained prior to measurement.

2.3. Multi-contrast image formation

2.3.1. Scattering OCT, birefringence, DOPU tomographies, and OCT-A

Four contrasts, the scattering OCT, birefringence, DOPU, and OCT-A, were computed from the Jones matrix tomographies as follows.

A sensitivity-enhanced scattering OCT was obtained by a coherent composition of the four repeated Jones matrix tomographies as described in Section 3.8 of [27].

The depth-resolved birefringence (local retardation) tomography was obtained by local Jones matrix analysis [24] combined with a maximum *a posteriori* birefringence estimator [25]. For easy observation, a pseudo-color birefringence tomography is created by combining the scattering intensity, birefringence, and reliability of the birefringence estimation. In this image, the birefringence is expressed by color hue if it is reliable, otherwise the pixel is a shade of gray. The birefringence computation protocol is detailed in Section 4 of [22], and the pseudo-color image formation is described in Section 3.4 of [25].

The DOPU image was obtained using the DOPU computation algorithm with Makita's noise correction [41].

To compute OCT-A signal, we first corrected detection jitter of spectral signal as described in the next section (Section 2.3.2). The jitter-corrected signal was then processed by a complex correlation based OCT-A method, which is detailed in Section 4.2 of [42].

Biomedical Optics EXPRESS

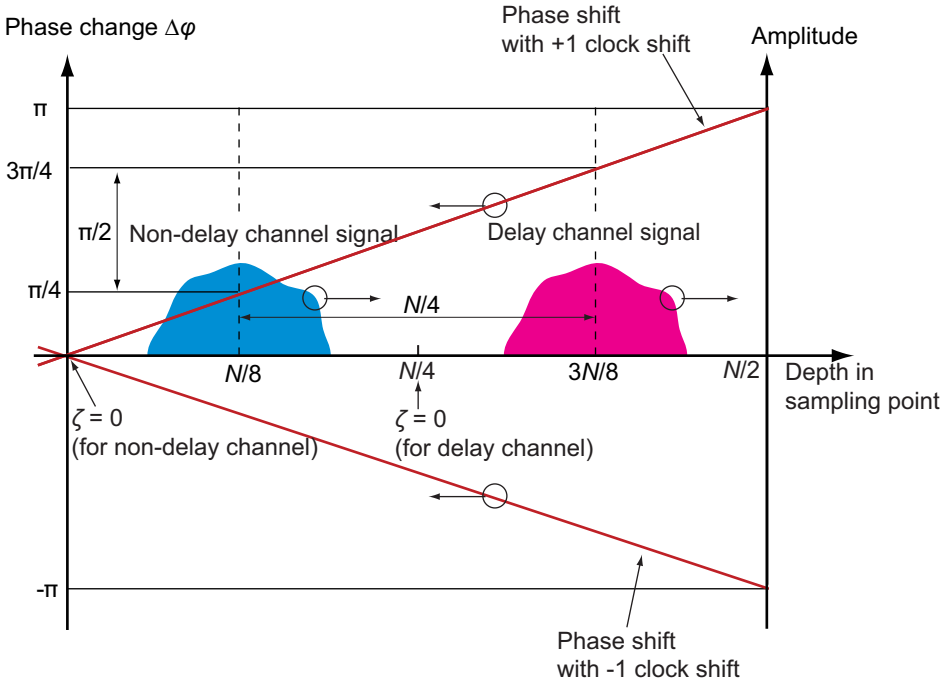

Fig. 2. Schematic diagram of the phase shift caused by the random shift of the spectral sampling signal. N is sampling number and ζ is indexed depth position. The 0-th sampling point corresponds to the zero depth of the non-delayed polarization channel, while $N/4$-th sampling point corresponds to that of delayed polarization channel. The upper and lower red lines indicate a phase error caused by jitter of +1 and -1 clock shifts, respectively. For the +1 clock shift, the delayed signal is phase shifted by $+\pi/2$ in respect to the non-delayed channel. For the -1 clock shift, the corresponding phase shift is $-\pi/2$.

2.3.2. Spectral jitter correction for OCT angiography

OCT-A images were obtained using a complex correlation-based OCT-A method, in which the noise-corrected complex correlation among the four repeated frames is computed. The details of this method are described elsewhere [42], but we additionally applied a jitter correction as follows.

The jitter is a random ±1-sampling-point spectral shift generated by a small mutual fluctuation between the k-clock and the A-trigger. It results in strong artifacts in OCT-A because the jitter generates a large difference between the two temporal phase changes of the two incident polarization images as schematically depicted in Fig. 2. Here, the two incident polarizations are denoted as non-delayed and delayed channels.

As the first step of the numerical jitter correction, we computed

$$\rho_{h,v}^{d,nd}(t,\zeta;\tau) \equiv \Gamma_{h,v}^{d,nd}(t+\tau,\zeta)\Gamma_{h,v}^{*d,nd}(t,\zeta), \tag{1}$$

where ζ is the depth-pixel index, t is time, and τ is a time-lag between repeated scans. Further, $\Gamma_{h,v}^{d,nd}(t,\zeta)$ is a complex OCT A-line at time t and at indexed depth ζ. Subscripts h and v represent the two polarization detection channels (horizontal and vertical) and superscripts d and nd represent the two incident polarizations (delay and non-delay). Superscript $*$ denotes the complex conjugate.

For each A-scan, we find five depth-points $(\zeta_1, \cdots, \zeta_5)$ with the highest time correlation using the method described in Section 3.1.1 of Ref. [42]. The temporal phase difference between

Biomedical Optics EXPRESS

$\Gamma^{d,nd}_{h,v}(t+\tau,\zeta)$ and $\Gamma^{d,nd}_{h,v}(t,\zeta)$ is then defined from the summation of $\rho^{d,nd}_{h,v}$ over the five points and the horizontal and vertical channels as

$$\Delta\phi^{d,nd}(t;\tau) \equiv \mathrm{Arg}\left[\sum_{i=1}^{5}\sum_{j=h,v}\rho^{d,nd}_{j}(t,\zeta_i;\tau)\right]. \tag{2}$$

Here, note that the spectral sampling jitter among A-lines is the −1, 0 or +1 sampling point. In addition, the delay between non-delay and delay channels was configured to be quarter of the sampling points (N). Hence, the phase difference between the delay and non-delay signals, $\Delta\varphi(t;\tau) \equiv \Delta\phi^{d}(t;\tau) - \Delta\phi^{nd}(t;\tau)$, takes only three possible values as $-\pi/2$ for the −1-sampling-point shift, 0 for the 0-sampling-point shift, and $\pi/2$ for +1-sampling-point shift. Hence, the amount of jitter m (in sampling points) is estimated as

$$m(t;\tau) \equiv \begin{cases} -1 & \text{if } \Delta\varphi(t;\tau) \simeq -\pi/2 \\ 0 & \text{if } \Delta\varphi(t;\tau) \simeq 0 \\ +1 & \text{if } \Delta\varphi(t;\tau) \simeq +\pi/2 \end{cases}. \tag{3}$$

Finally, the jitter corrected complex OCT signals are defined as

$$\hat{\Gamma}^{nd}_{h,v}(t+\tau,\zeta) \equiv \Gamma^{nd}_{h,v}(t+\tau,\zeta)\exp\left\{-i\frac{2\pi}{N}m\zeta\right\} \tag{4}$$

$$\hat{\Gamma}^{d}_{h,v}(t+\tau,\zeta) \equiv \Gamma^{d}_{h,v}(t+\tau,\zeta)\exp\left\{-i\frac{2\pi}{N}m\zeta - i\frac{\pi}{2}m\right\}, \tag{5}$$

where the first terms in the exponential in Eqs. (4) and (5) are for phase slope correction, and the second term in Eq. (5) is to correct a phase offset caused by the jitter. The OCT-A was finally computed by means of a complex correlation based OCT-A method [42] from these jitter-corrected OCT signals.

Figure 3 demonstrates the performance of the jitter correction. Without jitter correction, vertical low correlation (white) line artifacts are evident in the cross-sectional image [Fig. 3(a)] and several low correlation (white) salt-and-pepper artifacts appeared in the *en face* image [Fig. 3(b)]. These artifacts were removed by the jitter correction as shown in Figs. 3(c) and 3(d). The residual horizontal white artifacts in Fig. 3(d) are due to sample motion.

3. Results

3.1. Multi-contrast imaging of the outer-forearm

Examples of multi-contrast imaging of the skin of the outer-forearm are shown in Fig. 4. The cross-sectional images and *en face* images of each contrast were extracted from volumetric OCT data. The straight sloped lines above the surface of the skin that can be observed in the cross-sectional images [Figs 4(a)-(d)] are from the glass slip. The space between the glass slip and the skin surface was filled with ultrasound gel for refractive index matching. Small hyper-scattering spots in the gel [Fig. 4(a)] are the cross-sections of hairs.

Figure 4(a) is a cross-sectional scattering OCT. The epidermis appears as a relatively low scattering region just beneath the skin surface. The higher scattering region beneath the epidermis is dermis. Figure 4(b) is a complex-correlation OCT-A. The white (low time correlation) spots with tailed artifacts are blood vessels in the dermis. Figure 4(c) is the cross-sectional DOPU image. The epidermis and superficial part of the dermis (papillary dermis) appeared with high uniformity (red), while the uniformity decreases (yellow to green) in the deeper dermis. Figure 4(d) shows the birefringence property of the skin. The epidermis regions have low birefringence (blue), while the dermis regions have relatively high birefringence (green). It should be noted that

Biomedical Optics EXPRESS

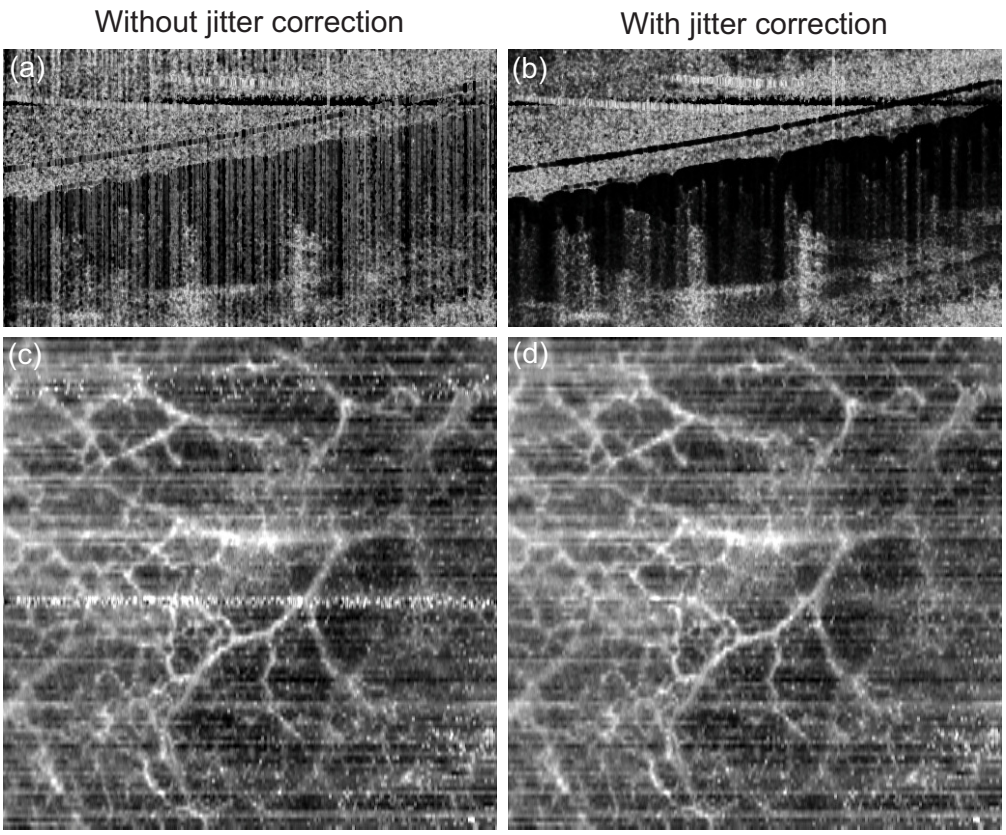

Fig. 3. Examples of OCT-A images of nail bed skin without (left) and with (right) motion correction. (a) and (b) are cross-sections, (c) and (d) are *en face* images.

regions with very low OCT signal, such as air and deep tissue regions, show not very low but only moderately low DOPU values. It is because the DOPU we used is not the original DOPU [40] but M-DOPU, which is DOPU with signal-to-noise ratio correction [41].

The *en face* slices [Figs. 4(e)-(h)] were extracted at the dermal level; 0.58-mm (in tissue) below the skin surface. The depth position of the slices is indicated by dashed lines in Figs. 4(a)-(d). Note that the texture pattern that appears in the scattering OCT [Fig. 4(e)] is not correlated with that in the DOPU [Fig. 4(g)]. Future histological correlative study is necessary for understanding these structures. The *en face* OCT-A [Fig. 4(f)] shows large plexus dermal vessels.

3.2. Multi-contrast imaging of finger pad

Figure 5 shows multi-contrast tomographies of the finger pad. In the backscattering OCT intensity image [Fig. 5(a)], the stratum corneum appears as the top most thick moderately scattering layer. The helical structures in the stratum corneum are sweat glands. In Fig. 5(c), the sweat glands appear with high polarization uniformity (red). The superficial part of the stratum corneum shows high polarization uniformity (red), while the lower part exhibits low polarization uniformity (yellow to green). In Fig. 5(b), the superficial stratum corneum exhibits low birefringence (blue to light blue). Since the superficial stratum corneum with distinctive DOPU and birefringence appearance is significantly thicker than the optical resolution and DOPU kernel, this superficial layer would not be an artifact. It would highlight inhomogeneity of stratum corneum as it can be seen in histology (i.e., Chapter 9 of [47]). The tissue beneath the stratum corneum is deeper

Biomedical Optics EXPRESS

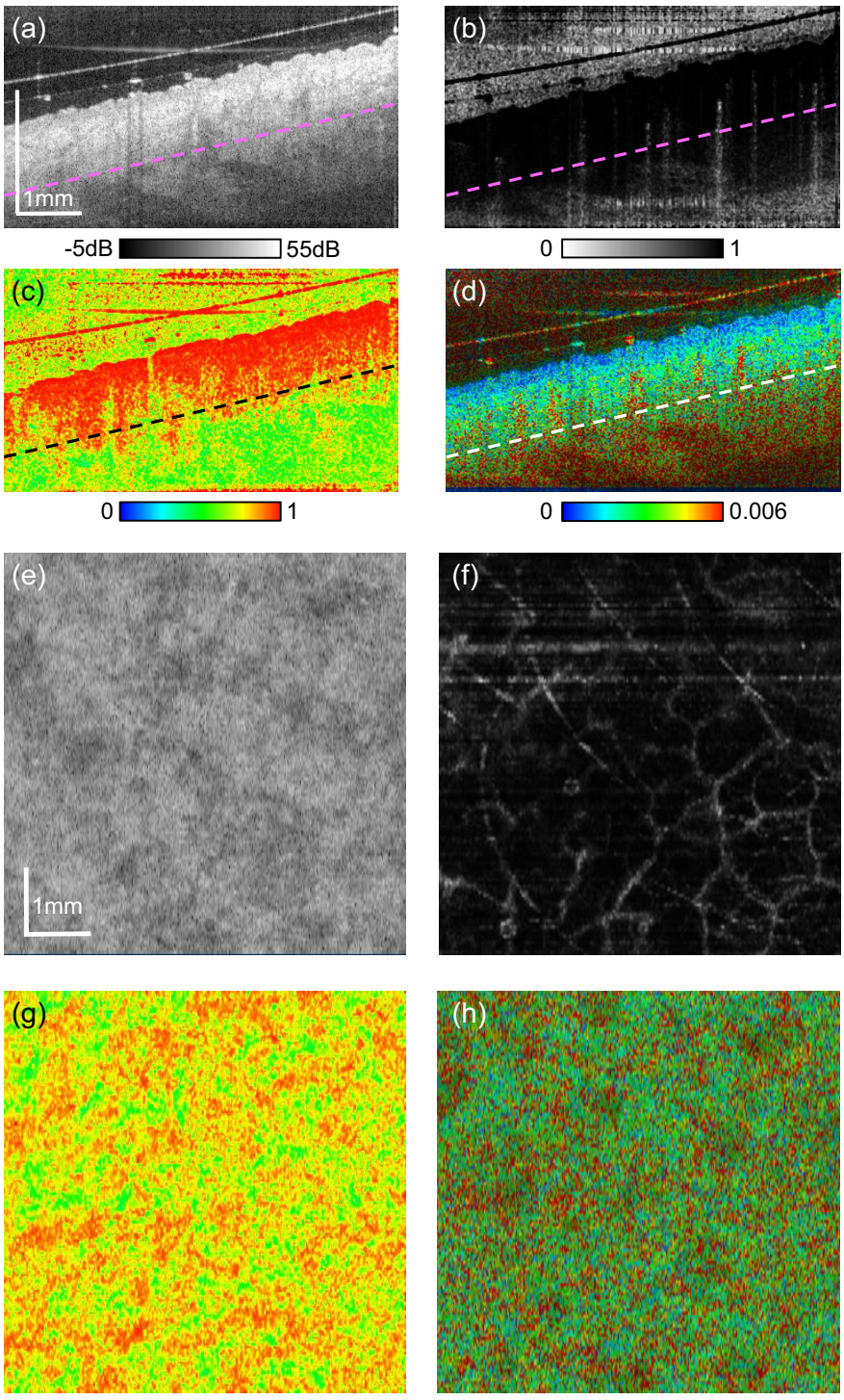

Fig. 4. Multi-contrast images of outer-forearm skin. Cross-sections of (a) scattering OCT, (b) OCT-A, (c) DOPU, and (d) birefringence. *En face* slices of (e) scattering OCT, (f) OCT-A, (g) DOPU, and (h) birefringence. The depth position of the *en face* slices are indicated by dashed lines in (a)-(d).

Biomedical Optics EXPRESS

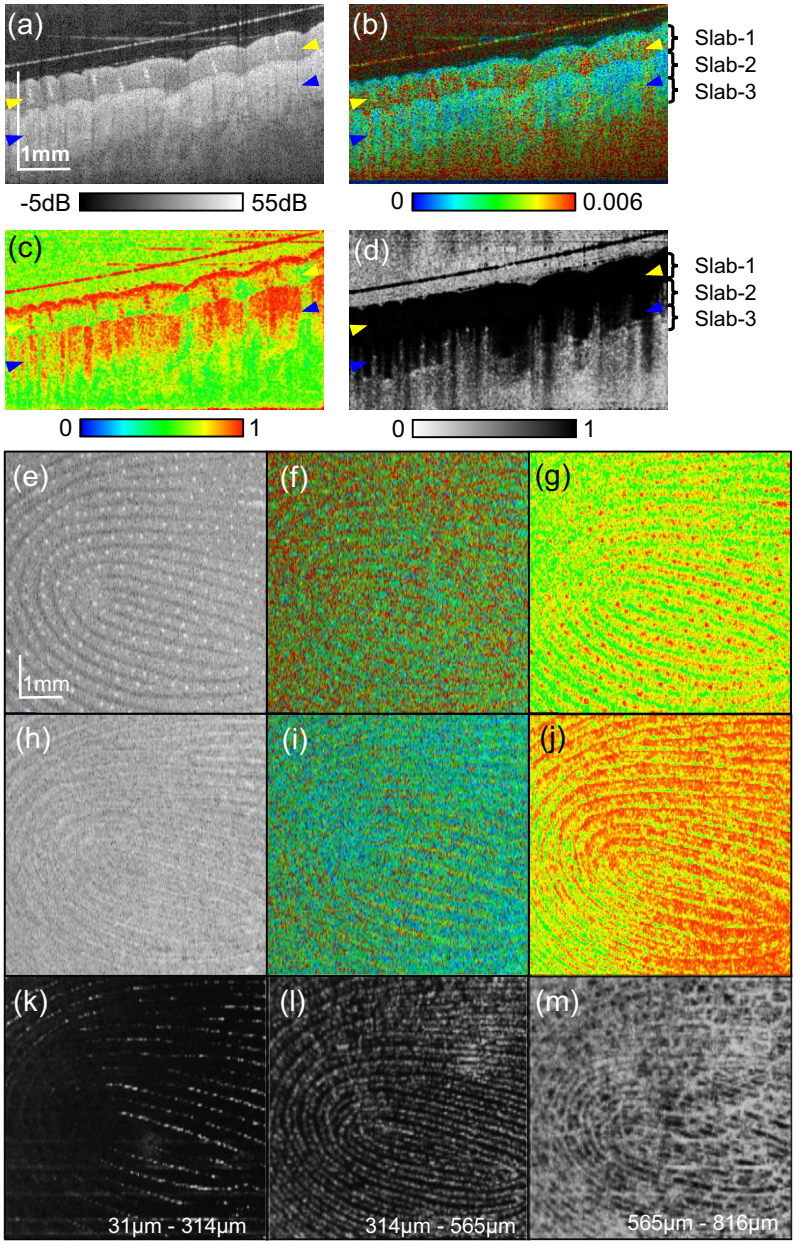

Fig. 5. Multi-contrast images of finger pad. Cross-sectional (a) intensity, (b) birefringence tomography, (c) DOPU tomography, and (d) OCT-A. (e)-(g) are *en face* slices at the depth indicated by yellow arrowheads in the cross-sectional images. (h)-(j) are *en face* slices at the depth of blue arrowheads. (e) and (h): scattering intensity, (f) ang (i): birefringence, (g) and (j): DOPU. (k)-(m) are slab projections of OCT-A. The depth positions of the slabs are indicated in (b) and (d).

Biomedical Optics EXPRESS

part of epidermis and then dermis, although these layers are not clearly distinguishable in a conventional OCT contrast image [Fig. 5(a)]. This region has weak to moderate birefringence (light blue to green) [Fig. 5(b)] and low polarization uniformity [Fig. 5(c)]. In the OCT-A cross section [Fig. 5(d)], some white spots appeare in the dermal region. Because the spots appeared with tailed artifacts, they are blood vessels. There is a diffuse white appearance in the deep (reticular) dermal region. It would indicate flows in capillaries.

The high birefringence appearance at the glass surface [Fig. 5(b)] would be an artifact caused by the birefringence computation method. In our method, the birefringence is computed by using two pixels separated for 6 pixels in depth. On the other hand, the glass surface signal has a depth width of around 2.2 pixels, which is defined by the depth resolution. Since, the signal width is significantly narrower than the pixel separation for the birefringence computation, the birefringence obtained at the glass surface cannot be accurate.

Bonesi *et al.* also investigated DOPU distribution of human fingertip (Fig. 6 of [36]. Since Bonesi *et al.* uses conventional DOPU [40] and we have used DOPU with Makita's noise correction [41], the absolute DOPU values are different. However, the overall tendency of DOPU values are consistent. For example, the superficial part of stratum corneum has very high DOPU and the middle layer of stratum corneum has low DOPU. In both images, the lower epidermal and dermal regions show vertical stripe patterns of DOPU as the ridge regions show higher DOPU than groove regions. Pircher *et al.* investigated the phase retardation and optic axis orientation appearances of finger pad [48]. Although this study did not use DOPU, the overall polarization-uniformity property of the finger pad are consistent with the present study. Namely, the phase retardation and the axis orientation at the middle part of stratum corneum showed random pattern as in Figs. 2 and 4 of [48], while our result showed low DOPU at this region. Pircher *et al.* also performed quantitative analysis of cumulative phase retardation at the stratum corneum. It was recently found that the cumulative phase retardation is not consistent with local phase retardation (birefringence) if the axis orientation is not constant (see Section 6.1 of [22]). Hence, it is hard to compare their phase retardation values and our birefringence values. In order to link the findings obtained by phase-retardation-based and birefringence-based PS-OCTs, it would be important to investigate the relationship among cumulative phase retardation, birefringence, and histology.

The *en face* images in Figs. 5(e)-(g) are at the 0.20 mm below the surface (stratum corneum, indicated by a pair of yellow arrowheads in the cross-sectional images) and Figs. 5(h)–(j) are 0.57 mm below the surface (around the superficial dermis, blue arrow heads). In the scattering OCT at the stratum corneum [Fig. 5(e)], the finger print appears with relatively bright bands (ridges) and dark bands (grooves). The bright spots aligned along the ridges are sweat ducts. In the DOPU image [Fig. 5(g)], the ridges appear with moderate uniformity (yellow) and the grooves appear with low uniformity (green). The sweat ducts appear as high-uniformity (red) spots in the ridges. In the scattering image of the deeper region [Fig. 5(h)], the bright bands (ridges) in the superficial layer appears as dark bands and the bright bands (grooves) appear as dark. This structure is known as the internal fingerprint [10]. The internal fingerprint is visible also in the DOPU image [Fig. 5(j)]. Unlike the superficial layer [Fig. 5(g)], the ridges appeard with high uniformity (red) and the grooves appear with low uniformity (yellow to green).

Figures 5(k)-(m) show the slab-average projection of OCT-A at the depths of 31 to 314 μm (stratum corneum, slab-1), 314 to 565 μm (deep epidermis to papillary dermis, slab-2), and 565 to 816 μm (deep dermis, slab-3), respectively. The depth locations of the slabs are indicated in Figs. 5(b) and 5(d). In the slab-2 [Fig. 5(l)], the vasculature forms the fingerprint pattern. This vasculature would be papillary capillaries, which are known to be aligned along the finger print ridges [49, 50]. Because slab-1 includes the deep epidermis and papillary dermis to some extent, some papillary capillaries are visible as shown in Fig. 5(k). The deepest slab (slab-3) [Fig. 5(m)] shows not only the fingerprint pattern but also the dermal vessel network.

Biomedical Optics EXPRESS

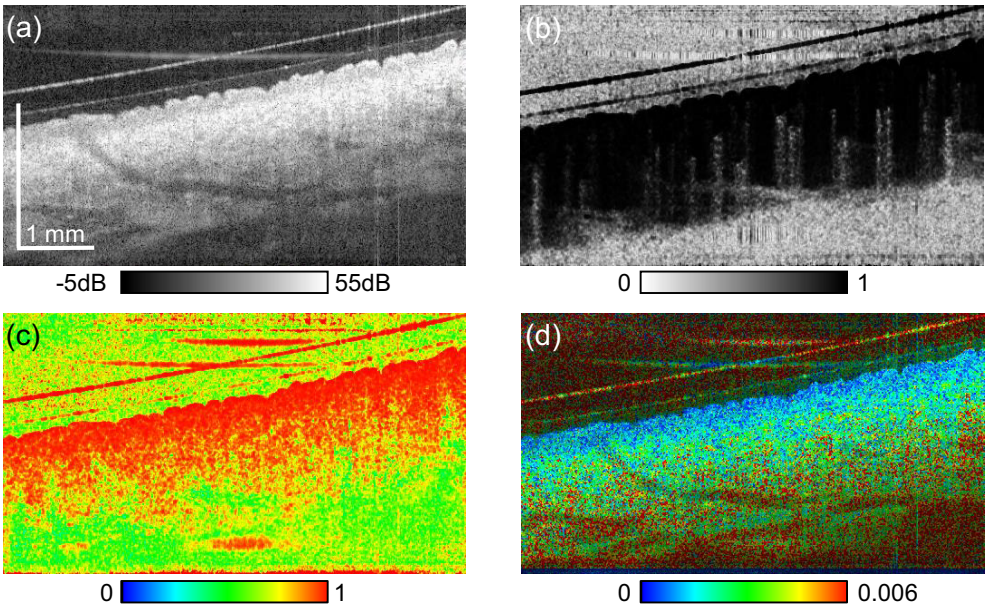

Fig. 6. Cross-sectional multi-contrast images of inner-forearm skin. (a) Scattering OCT, (b) OCT-A, (c) DOPU, and (d) birefringence tomography.

3.3. *Multi-contrast imaging of the inner-forearm*

The inner-forearm was measured as an example of thin skin. Figure 6 shows multi-contrast cross-sections of the forearm. In the scattering image [Fig. 6], the stratum corneum is appeared as the topmost thin hyper-scattering layer, which is significantly thinner than that of finger pad. The epidermis appears as relatively low scattering layer beneath the stratum corneum. It appears with high polarization uniformity (red) as shown in Fig. 6(c), while the dermis shows both low and high uniformity regions. The birefringence image [Fig. 6(d)] visualizes low birefringence (blue) in the epidermis, and moderately high birefringence (green) in the dermis. OCT-A [Fig. 6(c)] shows blood flow in the dermis. It should be noted that the very small high birefringence spots in Fig. 6(d) would be artifacts caused by birefringence measurement and/or estimation algorithm. One possible cause is that the current birefringence estimator [25] does not take the speckle effect into account. Although it was not evident as in Fig. 6(c), the same artifacts can also be seen in the birefringence images in Figs. 4 and 5.

We split the JM-OCT volume into three slabs based on its birefringence appearance as shown in Fig. 7, and OCT-A average projections were created for each slab [Figs. 7(b)–(d)]. The slabs show the low birefringence region (superficial slab), a mixture of low and high birefringence region (intermediate slab), and high birefringence region (deepest slab). The depths of each slab were 31 to 75 μm (superficial), 75 to 282 μm (intermediate), and 282 to 659 μm (deepest), respectively from the skin surface. The first superficial slab (low birefringence) had a thickness of around 75 μm, which is close to the epidermal thickness of the inner-forearm [51]. In the *en face* OCT-A of the first slab [Figs. 7(b)], vertical capillaries appear as white spots. The intermediate slab mainly consists of papillary dermis and its OCT-A shows fine vascular plexus [Figs. 7(c)]. The deepest slab also shows vascular plexus [Figs. 7(d)], but the vessels are thicker and the plexus is more macroscopic. See Visualization 1 of Fig. 7 for cut-away volumetric visualization.

Biomedical Optics EXPRESS

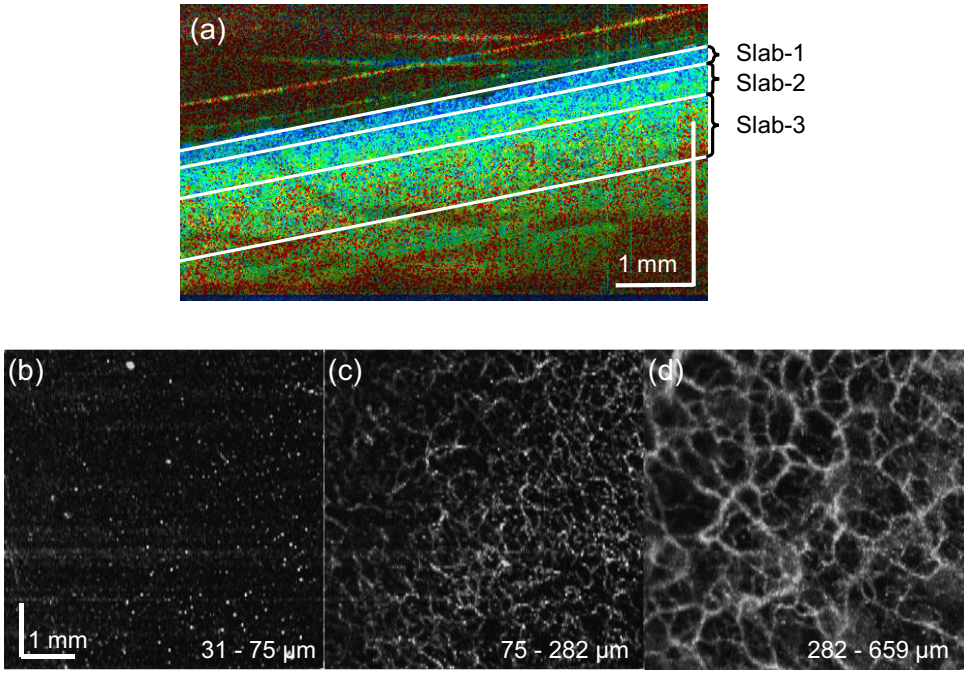

Fig. 7. (b)-(d) Slab projections of OCT-A of the inner-forearm skin tissue. The depth positions of the slabs are indicated in a cross-sectional birefringence tomography (a). See Visualization 1 for cut-away volumetric visualization.

4. Discussion and conclusion

Almost all previous PS-OCT studies used phase retardation imaging to investigate collagen-related skin alteration and optical properties, such as age-related alteration and photo-aging [19], and some mechanical skin properties [52]. Because birefringence imaging enables a more accurate and quantitative evaluation of tissue property than the phase retardation images [22], it will enable further investigation of skin properties, alteration, and pathologies.

There are still some limitations in the current JM-OCT. First, the imaging range is not always large enough. The depth measurement range of the current system is 2.5 mm in air (1.8 mm in tissue). This is sufficient for most tissue types, but it is not enough for tissue with a markedly uneven surface. In the current measurement protocol, we use a glass slip primarily to avoid skin surface reflection, but it also flattened the skin. Although this moderates the above limitation, it could potentially occlude the blood circulation, and hence, disturbs the OCT-A measurement. Hence, a JM-OCT with longer depth range is preferable. The measurement range is primarily limited by the k-clock frequency, and also by the coherence length of the wavelength sweeping light source. The former limitation can be resolved by using a high-frequency k-clock generator [28], and the latter can be resolved by using light sources with a more longer coherence length, such as akinetic light source [53] or VCSEL light source [54].

Another limitation is the relatively low lateral resolution in the out-of-focus region. This limitation will become more severe if we extend the depth measurement range as discussed above. Some possible solutions are numerical refocusing [55–58] or an extended focus technique [59–61].

The interpretation of birefringence values at low DOPU regions is an open issue. In this particular study, the birefringence is estimated by using a spatial kernel. So, the polarization property of the tissue is not uniform within the kernel and the estimated birefringence cannot be accurate. In other words, the estimated birefringence is not reliable if DOPU is low. This

Biomedical Optics EXPRESS

limitation should be considered for the interpretation of JM-OCT images.

In summary, we demonstrated dermatological multi-contrast OCT imaging using JM-OCT. Utilizing scattering, polarization, and flow contrasts, internal skin structures that were not visible by standard OCT could be visualized. Although there are still some limitations in this method, it also has several advantages including its non-invasiveness and three-dimensional measurement capability. It is expected that future studies will provide more evidences of its clinical utility.

Funding

This research was supported in part by the Japan Society for the Promotion of Science (JSPS, KAKENHI 15K13371) and the Japanese Ministry of Education, Culture, Sports, Science and Technology (MEXT) through a contract of Regional Innovation Ecosystem Development Program.

Acknowledgments

We would like to acknowledge Masahiro Yamanari and Satoshi Sugiyama for technical discussions. We also acknowledge Optohub for their great effort to build the compact passive polarization delay module and compact polarization diversity detector.

Disclosure

EL, SM, YJH, DK, YY: Topcon (F), Tomey Corp (F), Nidek (F), Canon (F)